

Prediction of the second peak in the afterglow of GW170817

Maxim V. Barkov,^{1,2*} Adithan Kathirgamaraju,¹ Yonggang Luo,¹
Maxim Lyutikov,¹ and Dimitrios Giannios,¹

¹ *Department of Physics and Astronomy, Purdue University, West Lafayette, IN 47907-2036, USA*

² *Astrophysical Big Bang Laboratory, RIKEN, 351-0198 Saitama, Japan*

Accepted XXX. Received YYY; in original form ZZZ

ABSTRACT

We performed calculations of the late radio and X-ray afterglow of GRB/GW170817 in the cocoon-jet paradigm, predicting appearance of a second peak in the afterglow light curve \sim one-three years after the explosion. The model assumes that the prompt emission and early afterglows originate from a cocoon generated during break-out of the delayed magnetically powered jet. As the jet breaks out from the torus-generated wind, a nearly isotropic mildly relativistic outflow is generated; at the same time the primary jet accelerates to high Lorentz factors and avoids detection. As the fast jet slows down, it should become visible to the off-axis observer. Thus, the model has a clear prediction: the X-ray and radio afterglows should first experience a decay, as the cocoon slows down, followed by a rebrightening when the primary jet starts emitting toward an observer.

Key words: keyword1 – keyword2 – keyword3

1 INTRODUCTION

On 2017 August 17, LIGO and Virgo detector discover the gravitational-wave (GW) transient GW170817 (LIGO Scientific Collaboration & Virgo Collaboration 2017), which was consistent with the coalescence of a binary neutron star system. Two seconds later GRB 170817A was registered by GBM/*Fermi* (Goldstein et al. 2017) and SPI-ACS/INTEGRAL (Savchenko et al. 2017) experiments. A the optical counterpart was detected by a large number of ground-based facilities (Abbott et al. 2017b).

GRB/GW170817 was unusual in many respects. The prompt gamma-ray emission consisted of two distinctive components - a hard short pulse delayed by ~ 2 seconds with respect to the LIGO signal followed by a weaker, softer thermal pulse with $T \sim 10$ keV lasting for another ~ 2 seconds, (see Fig. 1 in Pozanenko et al. (2018)). The appearance of a thermal component at the end of the burst is unusual for short GBRs. Both the hard and the soft components do not satisfy the Amati relation, making GRB 170817A distinctively different from other short GRBs (Pozanenko et al. 2018; Bromberg et al. 2018).

2 MODEL

The detection of the EM signal contemporaneous with gravitational waves is consistent with the binary NS scenario for short GRB (Blinnikov et al. 1984; Paczynski 1986; Eichler et al. 1989). Currently, there are several competing models for the prompt and afterglow emission from GW170817: (i) radially stratified quasi-spherical ejecta (*cocoon*) traveling at mildly relativistic speeds (e.g., Mooley et al. 2018; Kasliwal et al. 2017; Gottlieb et al. 2018); (ii) emission from off-axis collimated ejecta characterized by a narrow cone of ultra-relativistic material with slower wings extending to larger angles (*structured jet*) (e.g., Lamb & Kobayashi 2018; Troja et al. 2018b; D’Avanzo et al. 2018; Xie et al. 2018; Margutti et al. 2018; Kathirgamaraju et al. 2017; Lazzati et al. 2017). In the *structured jet* scenario, the GW170817 merger powered a normal SGRB directed away from the line of sight; (iii) *fast jet – cocoon* model - we describe it next in more detail.

The key points of the *fast jet – cocoon* model is described in (Pozanenko et al. 2018); also see Fig 1. An active stage of a merger lasts ~ 10 – 100 milliseconds after which the neutron stars collapse into BH. During the merger an accretion torus of $\sim 0.1M_{\odot}$ forms around the BH with a viscous time ~ 0.1 s (e.g. Ruiz et al. 2016; Perego et al. 2017). At the

* E-mail: mbarkov@purdue.edu (BMV)

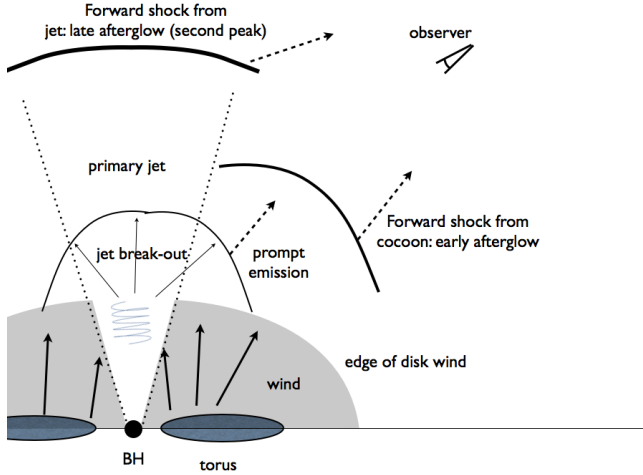


Figure 1. Cartoon of the model. Hot torus (left from the disrupted neutron stars) creates a dense, mildly relativistic wind (shaded region). After ~ 1 second, when enough magnetic flux is accumulated on the BH, the BH launches a Blandford-Znajek-powered jet. After the jet reaches the edge of the confining wind its head part experiences a break-out, creating a nearly spherical outflow; this generates the prompt emission. Later on, the interaction of this now nearly-spherically expanding part of the jet with the surrounding medium generates the forward shock - this leads to the production of early the early afterglow that has been observed so far. Most of the jet accelerates to high Lorentz factors; the radiation from the corresponding forward shock is beamed away from the observer. Only after the jet-driven forward shock decelerated it will become visible, and should generate the late bump in the afterglow.

same time, magnetic fields are amplified within the disk to $\sim 10^{15}$ G (Rezzolla et al. 2011; Lehner et al. 2012; Ruiz et al. 2016) due to the development of MRI and the presence of the velocity shear. Qualitatively, as the matter is accreted onto the BH, the BH accumulates magnetic flux. At the same time baryons slide off into the BH along magnetic field lines, leaving polar regions with low density. This creates conditions favorable for the operation of the Blandford-Znajek (BZ) mechanism (Blandford & Znajek 1977). As a result, the accumulation of the magnetic flux leads to a delay for the jet to switch-on. The BZ jet then propagates through a pre-existing dense wind with mildly relativistic velocity (Pozenenko et al. 2018; Bromberg et al. 2018). As it breaks out from the wind, it generates a nearly isotropic cocoon, Fig. 1. The wind emission shocked by the breaking-out jet produces the soft tail. After the break-out the primary jet accelerates and becomes invisible to the observer. The inclination of the binary system come directly from the GWs signal $\theta_{\text{obs}} \approx 30^\circ \pm 10^\circ$ (Abbott et al. 2017b; Finstad et al. 2018).

Observationally, Chandra and VLA (Troja et al. 2017, 2018a; Margutti et al. 2018; Alexander et al. 2018) show that GRB/GW170817 was steadily brightening with time, and have now reached its peak and starts to decay. The very simple power-law spectrum was extending for eight orders of magnitude in frequency. The measurement of the power law index $p = 2.17$ indicates that radiation should come from ejecta with $\Gamma \sim 3 - 10$.

We interpret these observations as non-thermal syn-

chrotron emission coming from the “break-out” (nearly spherical) part of the mildly relativistic forward shock. But observations up to $t \leq 250$ days have not been able to distinguish the above scenarios, because of the observed emission will be dominated by radiation from mildly relativistic material (Margutti et al. 2018) present in all the models.

Most importantly, at later times *the models predict qualitatively different behavior*. Both the *cocoon* and *structured jet* models should produce only one bump in X-ray light curve by the jet or the cocoon. On the other hand, the *fast jet - cocoon* model (Pozenenko et al. 2018) has two active components - a cocoon formed during jet breakout and an ultra-relativistic jet. The initial rise of x-ray light curve (see red dots Figure 3) is formed by a cocoon - a shock break-out. As we discuss in this paper, later on - a few years after GW event - the *fast jet - cocoon* model predicts rebrightening of the afterglow as the primary jet slows down and becomes visible (see Fig. 1). The detection of second X-ray or radio bump will be a smoking gun for *fast jet - cocoon* model and rule out one component models. Calculations of the properties of the predicted second afterglow bump is the key point of the paper.

3 RESULTS

In this work we perform three types of calculations of the predicted second peak: (i) using analytical estimates from (Nakar et al. 2002; Granot et al. 2017, §3.2); (ii) model light curves from the Afterglow library (van Eerten & MacFadyen 2012a, §3.3); (iii) in-house numerical calculations of the synchrotron emissivity of the relativistically expanding and synchrotron cooling plasma, §3.4.

3.1 The fiducial parameters

The accretion torus/disc after the NS-NS merger can be relatively massive $\sim 0.1M_\odot$ (e.g. Perego et al. 2017). The disc produces a dense mildly relativistic wind with mass $\sim 0.05M_\odot$ (Blandford & Begelman 1999; Metzger et al. 2008) and also supplies the central BH with magnetic flux needed to launch the BZ jet. The accretion rate on BH horizon can be estimated as (see more details in Pozenenko et al. 2018)

$$\dot{M}_{\text{BH}} \approx 0.002 \frac{M_{\text{d},-1}}{t^{5/3}} M_\odot/\text{s}. \quad (1)$$

Here $M_{\text{d}} = 0.1M_{\text{d},-1}M_\odot$ is mass of the disc in solar mass units and time is in seconds. The BZ jet power can be (Blandford & Znajek 1977; Barkov & Komissarov 2008; Barkov & Pozenenko 2011) as high as

$$L_{\text{BZ}} \approx 5 \times 10^{50} \frac{M_{\text{d},-1}}{t_{0.3}^{5/3}} \text{ erg/s}, \quad (2)$$

here we assume efficiency of BZ jet formation $C(a_{\text{BH}}) \approx a_{\text{BH}}^{2.4}$ with BH spin parameter $a_{\text{BH}} = 0.7$ (Ruiz et al. 2016; Radice et al. 2016).

The opening angle of the jet is unknown. The second bump can be detected if jet is relatively narrow and powerful. Following (Pozenenko et al. 2018) the opening angle

of the jet can be assumed $\theta_j = 0.1 \approx 5^\circ$, so the isotropic jet power can be as high as

$$E_{\text{iso,max}} \approx \frac{2}{\theta_j^2} \int_{t=2}^{\infty} L_{\text{BZ}} dt \approx 10^{53} \text{ ergs.} \quad (3)$$

This is the estimate of the primary jet energy that we will use in the calculations.

Initially, the primary jet emission is beamed away from the observer. As the jet-driven blast wave slows down it becomes visible. In the following, we perform calculations to address the question: What are the conditions required to produce an observable second afterglow bump from the primary jet.

3.2 Analytic estimates for detectability of the second peak.

Let us first obtain simple analytic constraints on parameters in order for the second peak associated with the afterglow of the jet to be detectable. We consider the second peak to be detectable if the following 3 criteria are satisfied. 1) The time of the second peak (t_{peak}) must be greater than the time of current observations (~ 250 d), otherwise this peak would have been already detected or can be weaker than the cocoon component, in which case the second peak will not be detectable. 2) The peak flux must be greater than the sensitivity limit of the detector (for radio at 6 GHz we use a limit of $10 \mu\text{Jy}$). 3) The value of the peak flux must be larger than that of the cocoon at the time of the peak. To estimate the flux from the cocoon component at a late time, we use a power law extrapolation of current observations. These criteria are depicted in the top panel of Fig. 2 where the numbered arrows show the regions where the corresponding criteria mentioned above are satisfied. In this figure we use the radio data at 6GHz as an example, the dashed vertical line marks a time of 250 days, the dot-dashed horizontal line marks a detectability limit of $10 \mu\text{Jy}$, and the solid line shows the extrapolation of the decline in the observed emission assuming it is $\propto t^{-2}$ as estimated in Alexander et al. (2018). Below we always assume the observing frequency $\nu_m < \nu < \nu_c$ and $(1+z) \approx 1$ which is valid for GW170817.

The peak in the afterglow occurs as the beaming angle of the emission from the core of the jet increases and reaches the line of sight of the observer ($1/\Gamma \sim \theta_{\text{obs}}$). This peak occurs at a time (e.g., Granot et al. 2017)

$$t_{\text{peak}} \approx 280 \left(\frac{E_{\text{iso},52}}{n_{-4}} \right)^{\frac{1}{3}} \left(\frac{\theta_{\text{obs}}}{25^\circ} \right)^{\frac{8}{3}} \text{ days.} \quad (4)$$

Criterion 1) requires $t_{\text{peak}} \gtrsim 250d$, using the above equation and assuming $\theta_{\text{obs}} = 25^\circ$, we get $E_{\text{iso},52} \gtrsim 0.8 n_{-4}$. This inequality is satisfied by all the regions above the dashed black line in the bottom panel of Fig. 2 which shows E_{iso} vs n .

The peak flux of the afterglow can be obtained by substituting t_{peak} in analytic expressions for the flux for post jet break light curves (e.g., Nakar et al. 2002; Granot et al. 2017)

$$F_{\text{peak}} \approx C(p) (1 - \cos\theta_j)^{\frac{p+3}{3}} \times$$

$$D_{\text{L},26}^{-2} \epsilon_{e,-1}^{p-1} \epsilon_{B,-2}^{\frac{p+1}{4}} n^{\frac{1+p}{4}} \theta_{\text{obs}}^{-\frac{8p}{3}} E_{\text{iso},52} \nu_{9.7}^{\frac{1-p}{2}} \text{ mJy,} \quad (5)$$

Where θ_{obs} is in degrees and

$$C(p) \approx 7440(p - 0.04) \left(\frac{p-2}{p-1} \right)^{p-1} \left(1.13 \times 10^{-20} \right)^{-p} 10^{-14.96p}$$

These analytic estimates agree within a factor ~ 1.5 when compared to the light curves shown in Fig. 3. Criterion 2 requires F_{peak} to be larger than the detector sensitivity, in the case of radio we use $F_{\text{peak}} \gtrsim 0.01$ mJy. Substituting $\epsilon_e = 0.1$, $p = 2.17$, $\nu = 6$ GHz, $\theta_{\text{obs}} = 25^\circ$, $\theta_j = 5^\circ$, $D_{\text{L}} = 40$ Mpc, criterion 2 yields

$$E_{\text{iso},52} \gtrsim 0.4(n_{-4} \epsilon_{B,-2})^{-0.79}. \quad (6)$$

This condition is shown by the dot-dashed line in the bottom panel of Fig. 2, where the different colors corresponds to different values of $\epsilon_B = 10^{-2}, 10^{-3}, 10^{-4}$ as indicated in the plot legend. The regions above the dot-dashed lines satisfy criterion 2 for the corresponding values of ϵ_B .

The final criterion for detectability requires that the flux at peak, F_{peak} is larger than the flux from the cocoon component. The latest observations show the afterglow of GW170817 has started to decline, and this decline follows a power law in time as roughly $\propto t^{-2}$ (Alexander et al. 2018). Attributing this emission to the cocoon, we estimate the late time flux from it by extrapolating this power to later times. For example, taking the 6 GHz measurements we can model the decline in flux as

$$F_d(t) \approx 0.018 t_{2.5}^{-2} \text{ mJy,} \quad (7)$$

with t in days. This extrapolation is shown by the solid line in the top panel of Fig. 2. Criterion 3 requires $F_{\text{peak}} > F_d(t_{\text{peak}})$. Using the same parameter substitutions used to obtain equation 6, this condition yields

$$E_{\text{iso},52} \gtrsim \epsilon_{B,-2}^{-0.476} n_{-4}^{-0.0755}. \quad (8)$$

This equality is shown by the solid lines in the bottom panel of Fig. 2 where different colors correspond to different values of ϵ_B color coded in the same way as for criterion 2 (the dot-dashed lines). Therefore the inequality 8 is satisfied for regions above the solid lines. So the regions in Fig. 2 which satisfy all three criteria must lie above the dashed black line (criterion 1), and above the dot-dashed and solid lines (criterion 2 and 3) corresponding to the same value of ϵ_B . These regions have been shaded for better visualization. In order for the second peak to be detectable, the parameters pertaining to the jet must lie in the shaded regions.

3.3 Second peak light curves using the ‘‘Afterglow library’’

In this Section we discuss the calculations of the afterglow light curves using the ‘‘Afterglow library’’ (van Eerten & MacFadyen 2012a), which uses linear radiative transfer to calculate synchrotron light curves and spectra. We use a few different sets of parameters when calculating the afterglow (maybe point to a table or plot listing the parameters). Guided by observations (references), we fix the spectral slope, $p = 2.17$ and the observing angle w.r.t jet axis, $\theta_{\text{obs}} = 25^\circ$. We use a typical value of $\epsilon_e = 0.1$, which denotes the fraction of energy in the electrons of the shocked fluid, and a relatively narrow ‘top-hat’ jet with opening angle $\theta_j = 5$ deg. We vary the isotropic equivalent energy E_{iso} ,

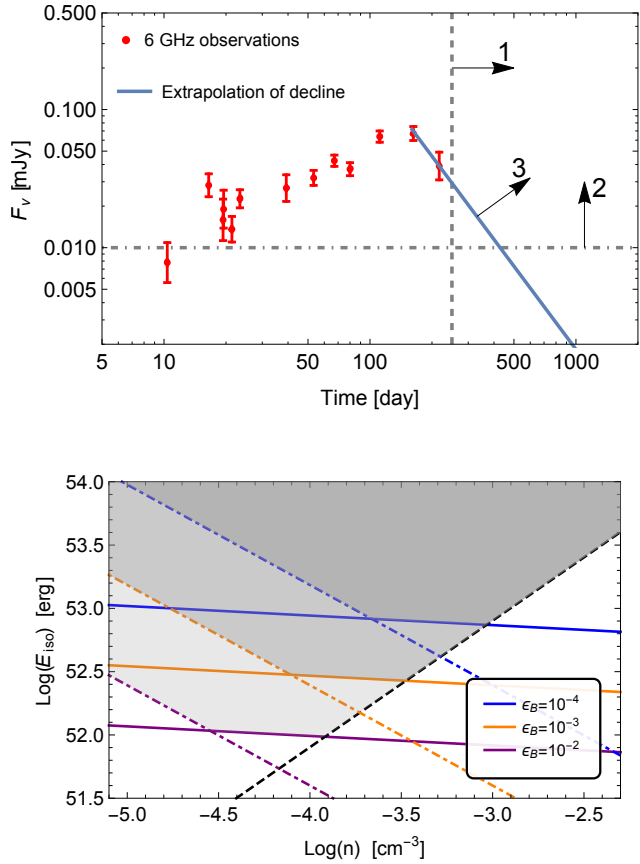


Figure 2. (Top) Depiction of the three criteria required for detectability of second peak. The plot shows observed radio data (red points) and a power law extrapolation of the observed decline (solid line) (data taken from [Margutti et al. 2018](#); [Alexander et al. 2018](#)). Vertical dashed line marks a time of 250 days and dot-dashed horizontal line indicates a radio detectability limit of $10 \mu\text{Jy}$. The numbered arrows point to the region where the second peak must lie in order to be detectable and the numbers label the criteria described in Section 3.2. In short, 1) requires peak time to be greater than 250d, 2) requires peak flux be above detector sensitivity and 3) requires peak flux be larger than cocoon emission. (Bottom) A figure exploring the parameter space in isotropic equivalent energy of the jet (E_{iso}) vs. external density (n). Shaded regions mark the parameter space where the second peak will be detectable (where all 3 criteria mention in top panel and Section 3.2 are satisfied). Regions above dashed black line satisfy criterion 1, above dot-dashed lines satisfy criterion 2 and above solid lines satisfy criterion 3. Colors indicate the value of ϵ_B used for the solid and dot-dashed lines. See section 3.2 for analytic expressions of the lines, shaded regions and for relevant parameters used.

the fraction of energy in the magnetic field of the shocked fluid ϵ_B , and number density of external medium $n \text{ cm}^{-3}$. The resulting light curves for these different sets of parameters are shown in fig 3 the observations of GW170817 (taken from [Margutti et al. \(2018\)](#)) are also shown in the same plots for radio (6 GHz) and X-ray (1 keV). These plots demonstrate the possibility where the afterglow from the jet can cause a late time rise in the light curve of GW170817.

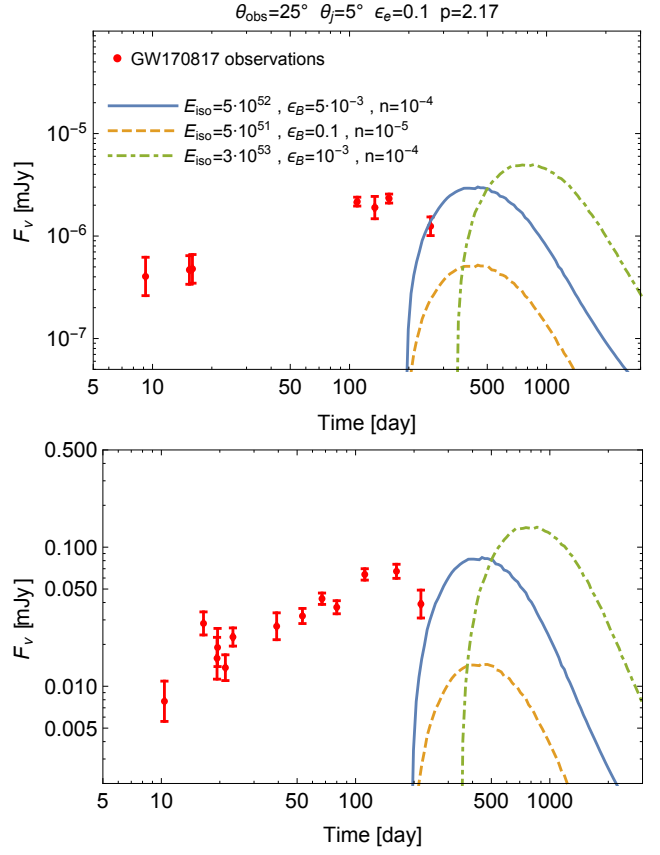


Figure 3. Light curves in X-ray at 1 keV (Top) and Radio at 6 GHz (Bottom) using the “Afterglow library”. Red points show observations of GW170817 ([Margutti et al. 2018](#)), and lines show the afterglow from a jet calculated using the afterglow library ([van Eerten & MacFadyen 2012b](#)) for two sets of parameters (see sec. for description of parameters). In a *fast jet – cocoon* model, the earlier time observations (red points) can be attributed to emission from the cocoon. The afterglow from a jet will peak at later times for off-axis observers, in this scenario, this peak can cause a second bump in the overall X-ray light curve of GW170817. For parameters used here, the second peak occurs at ~ 500 days.

3.4 Emission from off-axis forward shock: numerical calculation of synchrotron emission

Next, we use the classic forward shock model of [Sari et al. \(1996, 1998\)](#) to calculate the emission seen by an off-axis observer. As a novel feature, we calculate numerically the radiative and cooling losses of the particles. To do so, we first find Greens function for particles injected at some moment in time into the forward shock, then we integrate over different injections times, and allowing for time-of-flight delays we calculated the expected light curve.

We assume self-similar relativistic shock with $\Gamma \propto t^{-m/2}$ with $m = 3$ ([Blandford & McKee 1976](#)) (thus, we neglect lateral evolution of the shock - it is small, see [van Eerten et al. 2010](#); [Lyutikov 2012](#)). The minimum Lorentz factor of accelerated electrons in the shock frame is then

$$\gamma'_{\text{min}} \propto \epsilon_e (\Gamma - 1) \frac{m_p}{m_e}, \quad (9)$$

while the comoving magnetic field is

$$\frac{B'^2}{8\pi} = \epsilon_B n_p (\Gamma - 1) \Gamma m_p c^2 \propto t^{-m} \propto t'^{-\frac{2m}{2+m}} \quad (10)$$

(primed quantities are in the fluid frame and un-primed are in the coordinate frame.) Thus, the magnetic field strength satisfies

$$B' = B'_0 \left(\frac{t'}{t'_0} \right)^{-\frac{m}{m+2}} \quad (11)$$

where the magnetic field is B_0 and Lorentz factor is $\Gamma = \Gamma_0$ at time $t' = t'_0$.

Particles are injection with distribution function f_{inj} at time t'_i through an area A . The Lorentz factor of particles evolves according to

$$\begin{aligned} \frac{d\gamma'}{dt'} &= -\frac{\tilde{C}_2 B_0^2 \gamma'^2}{t'^{\frac{2m}{2+m}}} - \frac{m\gamma'}{2t'(2+m)} \\ \tilde{C}_2 &= \frac{\sigma_T t_0^{\frac{2m}{2+m}}}{6\pi m_e c} \end{aligned} \quad (12)$$

where the first term describes radiative losses and the second the adiabatic expansion.

The evolution of the distribution function is then described by, first, solving for the Greens function $G(\gamma', t', t'_i)$

$$\begin{aligned} \frac{\partial G(\gamma', t')}{\partial t'} &= \frac{\tilde{C}_2 B_0^2}{t'^{\frac{2m}{2+m}}} \frac{\partial (\gamma'^2 G(\gamma', t'))}{\partial \gamma'} + \frac{m}{2t'(2+m)} \frac{\partial (\gamma' G(\gamma', t'))}{\partial \gamma'} \\ &+ f'_{inj}(\gamma', t'_i) \delta(t' - t'_i) \end{aligned} \quad (13)$$

with injection

$$f'_{inj}(\gamma', t'_i) = f'_i \gamma'^{-p} \Theta(\gamma' - \gamma'_{\min}(t'_i)) \quad (14)$$

where f'_i satisfies $f'_i \int_{\gamma'_{\min}}^{\infty} \gamma'^{-p} d\gamma' = nAc$. And, second, integrating with the injection rate

$$f(\gamma', t') = \int G(\gamma', t', t'_i) f'_i dt'_i, \quad (15)$$

where $f(\gamma', t')$ is the total distribution.

Consider a jet (actually, a shock) with opening angle θ_j viewed at an angle θ_{obs} . Emissivity at each moment is given by an integral over the shock surface

$$\begin{aligned} L'(\omega', t') &= \int \int \frac{f(\gamma', t')}{A} P(\omega') d\gamma' dA \\ &\approx \int_{\theta_{\text{obs}} - \theta_j}^{\theta_{\text{obs}} + \theta_j} \int_{\phi_{\min}\theta}^{\phi_{\max}\theta} \int_{\gamma'_{\min}}^{\infty} \frac{r^2 \sin\theta f(\gamma', t') P(\omega')}{2\pi(ct'\Gamma)^2 (1 - \cos\theta_j)} d\gamma' d\phi d\theta \\ &= \int_{\theta_{\text{obs}} - \theta_j}^{\theta_{\text{obs}} + \theta_j} \int_{\gamma'_{\min}}^{\infty} \frac{(\phi_{\max}\theta - \phi_{\min}\theta) r^2 \sin\theta f(\gamma', t') P(\omega')}{2\pi(ct'\Gamma)^2 (1 - \cos\theta_j)} d\gamma' d\theta \end{aligned} \quad (16)$$

where f is the distribution function, P_ω is the synchrotron power per unit frequency emitted by each electron and we assumed that θ_{obs} is larger than θ_j

The photons emitted by different parts of the jet at the same moment will arrive at different time due to time-of-flight effects. The distance between the initial explosion point and an emission point (r, θ) is $r = vt(1 - \beta \cos\theta)^{-1}$, so the surfaces that corresponds to the instantaneous emission have relation:

$$r = vt = \frac{vT_0}{1 - \beta} = \frac{vT_{\theta_i}}{1 - \beta \cos(\theta_i)} \quad (17)$$

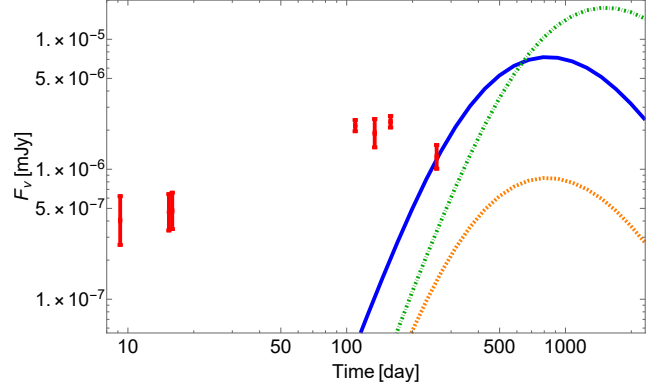


Figure 4. Light curves in X-ray at 1 keV using the radiative calculations, see text for details. Red points show the observation of GW170817 at 1 KeV (Alexander et al. 2018). All light curves have the same parameter value as Figure 3.

where T_0 represents the observe time at $\theta = 0$, and T_{θ_i} represents the observe time at $\theta = \theta_i$.

The time t is measured in lab frame; the corresponding observe time T_{obs} is a function of θ : $t = \frac{T_{\text{obs}}}{1 - \beta \cos\theta}$. So

$$\sin\theta d\theta = -\frac{T_{\text{obs}}}{t^2 \beta} dt \approx -\frac{T_{\text{obs}}}{t^2} dt \quad (18)$$

The geometric relation between θ and ϕ is

$$\phi_{\max}\theta - \phi_{\min}\theta = 2 \arccos\left(\frac{\cos\theta_j - \cos(\theta_{\text{obs}})\cos\theta}{\sin(\theta_{\text{obs}})\sin\theta}\right) \quad (19)$$

Using $t = t'\Gamma$, the equation (16) becomes

$$\begin{aligned} L' &\approx \int_{t'_{\theta'=\theta_{\text{obs}}-\theta_j}}^{t'_{\theta'=\theta_{\text{obs}}+\theta_j}} \int_{\gamma'_{\min}}^{\infty} -2 \arccos\left(\frac{\cos\theta_j - \cos(\theta_{\text{obs}})\cos\theta}{\sin(\theta_{\text{obs}})\sin\theta}\right) \times \\ &\frac{c^2 T_{\text{obs}} \Gamma f(\gamma', t') P(\omega')}{2\pi(ct'\Gamma)^2 (1 - \cos\theta_j)} d\gamma' dt' \end{aligned} \quad (20)$$

Taking into account Doppler boosting, we finally arrive at the equation for the observed spectral luminosity as function of the observer time

$$\begin{aligned} L &\approx \int_{t'_{\theta'=\theta_{\text{obs}}-\theta_j}}^{t'_{\theta'=\theta_{\text{obs}}+\theta_j}} \int_{\gamma'_{\min}}^{\infty} \arccos\left(\frac{\cos\theta_j - \cos(\theta_{\text{obs}})\cos\theta}{\sin(\theta_{\text{obs}})\sin\theta}\right) \times \\ &\frac{T_{\text{obs}} \delta^3 P(\frac{\omega}{\delta}) \int G(\gamma', t', t'_i) f'_i dt'_i}{\pi t'^2 \Gamma (1 - \cos\theta_j)} d\gamma' dt' \end{aligned} \quad (21)$$

where

$$T_{\text{obs}} = \frac{(2+m)t'}{(1+m)\Gamma} \quad (22)$$

Using the above procedure we calculate the light curve behavior at 1 keV for the same set of parameters as in Fig. 3, see Fig.4. Within a factor of a few the two methods produce similar results.

4 CONCLUSIONS

In this paper we argue that late afterglow of GRB/GW170817 may experience a second peak in brightness, as the fast primary jet, which avoided detection

so far, becomes visible. Using three different approaches – basic analytic estimates, “Afterglow library” and new radiative calculations – we put constraints on the jet energetics and microphysical parameters for the second peak to be observable.

Detectability of the second peak depends on macroscopic parameter (energy of the primary jet E_{iso} and external density n), as well as microscopic parameters (ϵ_e and ϵ_B), as well as the viewing angle. Observations of the prompt emission and the corresponding GRB constrain the viewing angle to be $\sim 20 - 30^\circ$ (e.g. Abbott et al. 2017a; Pozanenko et al. 2018; Alexander et al. 2018). Thus, we are left with E_{iso} , n and ϵ_e , ϵ_B .

Our results indicate that even a mildly energetic jet, with $E_{\text{iso}} \sim \text{few} \times 10^{51}$ ergs may be detected even for low external density $n \sim 10^{-5} \text{ cm}^{-3}$ (if ϵ_e and ϵ_B are not too small). This compares favorably with the expected jet power (3).

We end our conclusions with general remark: if the jet has more energy than the cocoon, it should show up as a second distinct peak. This is because the other parameters (n , ϵ_e , and ϵ_B) should actually be the same for the 2 afterglow components. In the case of radiatively inefficient jet, the late time emission just tracks the total true energy of the jet. We can even argue that since the jet drives the cocoon, it is typically true that $E_{\text{jet}} > E_{\text{cocoon}}$, i.e. we should see two bump structure on light curves from radio through X-ray.

ACKNOWLEDGEMENTS

This work had been supported by NSF grant AST-1306672, DoE grant DE-SC0016369 and NASA grant 80NSSC17K0757. DG and AK acknowledge support from NASA grants NNX16AB32G and NNX17AG21G.

REFERENCES

- Abbott B. P., et al., 2017a, *ApJ*, **848**, L12
 Abbott B. P., et al., 2017b, *ApJ*, **848**, L13
 Alexander K. D., et al., 2018, preprint, ([arXiv:1805.02870](https://arxiv.org/abs/1805.02870))
 Barkov M. V., Komissarov S. S., 2008, *MNRAS*, **385**, L28
 Barkov M. V., Pozanenko A. S., 2011, *MNRAS*, **417**, 2161
 Blandford R. D., Begelman M. C., 1999, *MNRAS*, **303**, L1
 Blandford R. D., McKee C. F., 1976, *Physics of Fluids*, **19**, 1130
 Blandford R. D., Znajek R. L., 1977, *MNRAS*, **179**, 433
 Blinnikov S. I., Novikov I. D., Perevodchikova T. V., Polnarev A. G., 1984, *Pis ma Astronomicheskii Zhurnal*, **10**, 422
 Bromberg O., Tchekhovskoy A., Gottlieb O., Nakar E., Piran T., 2018, *MNRAS*, **475**, 2971
 D’Avanzo P., et al., 2018, preprint, p. [arXiv:1801.06164](https://arxiv.org/abs/1801.06164)
 Eichler D., Livio M., Piran T., Schramm D. N., 1989, *Nature*, **340**, 126
 Finstad D., De S., Brown D. A., Berger E., Biwer C. M., 2018, preprint, ([arXiv:1804.04179](https://arxiv.org/abs/1804.04179))
 Goldstein A., Veres P., Burns E., et al. 2017, *ApJ*, **848**, L14
 Gottlieb O., Nakar E., Piran T., 2018, *MNRAS*, **473**, 576
 Granot J., Gill R., Guetta D., De Colle F., 2017, preprint, ([arXiv:1710.06421](https://arxiv.org/abs/1710.06421))
 Kasliwal M. M., et al., 2017, *Science*, **358**, 1559
 Kathirgamaraju A., Barniol Duran R., Giannios D., 2017, [ArXiv:1708.07488](https://arxiv.org/abs/1708.07488),

- LIGO Scientific Collaboration Virgo Collaboration 2017, LVC GRB Coordinates Network, 21505
 Lamb G. P., Kobayashi S., 2018, *MNRAS*, p. 1056
 Lazzati D., Perna R., Morsony B. J., López-Cámara D., Cantiello M., Ciolfi R., giacomazzo B., Workman J. C., 2017, preprint, p. [arXiv:1712.03237](https://arxiv.org/abs/1712.03237) ([arXiv:1712.03237](https://arxiv.org/abs/1712.03237))
 Lehner L., Palenzuela C., Liebling S. L., Thompson C., Hanna C., 2012, *Phys. Rev. D*, **86**, 104035
 Lyutikov M., 2012, *MNRAS*, **421**, 522
 Margutti R., et al., 2018, [ArXiv:1801.03531](https://arxiv.org/abs/1801.03531),
 Metzger B. D., Piro A. L., Quataert E., 2008, *MNRAS*, **390**, 781
 Mooley K. P., et al., 2018, *Nature*, **554**, 207
 Nakar E., Piran T., Granot J., 2002, *ApJ*, **579**, 699
 Paczynski B., 1986, *ApJ*, **308**, L43
 Perego A., Radice D., Bernuzzi S., 2017, *ApJ*, **850**, L37
 Pozanenko A. S., et al., 2018, *ApJ*, **852**, L30
 Radice D., Galeazzi F., Lippuner J., Roberts L. F., Ott C. D., Rezzolla L., 2016, *MNRAS*, **460**, 3255
 Rezzolla L., Giacomazzo B., Baiotti L., Granot J., Kouveliotou C., Aloy M. A., 2011, *ApJ*, **732**, L6
 Ruiz M., Lang R. N., Paschalidis V., Shapiro S. L., 2016, *ApJ*, **824**, L6
 Sari R., Narayan R., Piran T., 1996, *ApJ*, **473**, 204
 Sari R., Piran T., Narayan R., 1998, *ApJ*, **497**, L17
 Savchenko V., Ferrigno C., Kuulkers E., et al. 2017, *ApJ*, **848**, L15
 Troja E., et al., 2017, *Nature*, **551**, 71
 Troja E., et al., 2018a, [ArXiv:1801.06516](https://arxiv.org/abs/1801.06516),
 Troja E., et al., 2018b, *MNRAS*, p. L60
 Xie X., Zrake J., MacFadyen A., 2018, preprint, p. [arXiv:1804.09345](https://arxiv.org/abs/1804.09345) ([arXiv:1804.09345](https://arxiv.org/abs/1804.09345))
 van Eerten H. J., MacFadyen A. I., 2012a, *ApJ*, **747**, L30
 van Eerten H. J., MacFadyen A. I., 2012b, *ApJ*, **751**, 155
 van Eerten H., Zhang W., MacFadyen A., 2010, *ApJ*, **722**, 235

This paper has been typeset from a $\text{\TeX}/\text{\LaTeX}$ file prepared by the author.